https://doi.org/10.1007/s41230-025-4170-6

Effects of Cr element doping on microstructure and performance of quinary FeCoNiSiB multi-principal element alloys

Shu-yan Zhang[1], *Dan-yue Ma[2], **Pei-pei Shen[1], Bo Sun[3], Hua Chen[1], and Zhi-bin Zhang[4]

1. National Institute of Extremely-weak Magnetic Field Infrastructure, Hangzhou 310051, China

2. Key Laboratory of Ultra-Weak Magnetic Field Measurement Technology, Ministry of Education, School of Instrumentation and Optoelectronic Engineering, Beihang University, Beijing 100191, China

3. School of Materials Science and Engineering, Jiangsu Key Laboratory for Advanced Metallic Materials, Southeast University, Nanjing 211189, China

4. Defense Innovation Institute, Academy of Military Science, Beijing 100071, China

Abstract: This research focused on the influences of Cr element doping on the microstructure, thermal stability, microhardness, soft magnetic, and anti-corrosion properties of FeCoNiSiB multi-principal element alloys. The as-received Fe-Co-Ni-Si-B-Cr alloy ribbons made by melt-spinning technique could maintain amorphous nature. The glass-transition temperature and onset crystallization temperature become lower with the addition of Cr, and the highest values are 782.0 K and 821.5 K, respectively. When the Cr content reaches 3at.%, the alloy owns the best soft magnetic performance with the saturation magnetic flux density of ~0.578 T and coercivity of ~5.5 $A \cdot m^{-1}$ among the studied melt-spun ribbon samples. The microhardness of all alloy ribbons reduces with an increasing Cr content on the whole, and the values are 810 $HV_{0.5}$ or above. The corrosion behavior of these multi-principal element amorphous alloys containing Cr was also investigated in detail. As the Cr content increases, the corrosion resistance becomes superior and the specimens present the obvious passive regions in 3.5wt.% NaCl solution. The glassy ribbons with 8at.% Cr have the highest self-corrosion potential of –0.340 V and pitting potential of 0.288 V as well as the widest passive region of 0.628 V. Besides, the corroded micrographs of alloy ribbons immersed in corrosive environment lasting 100 h are also presented, which further confirms the above-mentioned experimental results. This research deepens the understanding about the role of Cr element in the microstructure and a series of physical and chemical properties of Fe-Co-Ni-Si-B-Cr multi-principal element amorphous alloys.

Keywords: multi-principal element amorphous alloys; microstructure; thermal stability; soft magnetic properties; corrosion resistance

CLC numbers: TG142 **Document code:** A **Article ID:** 1672-6421(2025)04-427-12

1 Introduction

Multi-principal element alloys (MPEAs), also named as medium/high entropy alloys (M/HEAs), usually consist of three or more components with nearly equal elemental ratios [1]. These kinds of alloys become a hot spot in the realm of metal materials and also pioneer a new frontier in the field of metallic materials owing to the potential outstanding and eye-catching performance brought by the extensive composition spaces [2-6]. Amorphous alloys have received increasing attention as advanced materials in recent decades and the first amorphous alloy of Au-Si has been discovered for over half a century. Amorphous alloys can be called metallic glasses (MGs) as well. Because of the unusual combination of excellent performance characteristics, such as exceptional corrosion resistance, high strength and hardness, good soft magnetic and fatigue properties, they are often considered as novel engineering alloys in

***Dan-yue Ma**

Born in 1994, Ph. D., Associate Professor. Her current research interests focus on the design of magnetic shielding, the suppression of magnetic noise, and the development of magnetic shielding materials.

E-mail: madanyue0419@buaa.edu.cn

****Pei-pei Shen**

E-mail: 13602127595@163.com

Received: 2024-08-11; Revised: 2024-09-04; Accepted: 2024-09-06

which the structure is not crystalline [7, 8]. Amorphous alloy with the nominal composition of $Fe_{80}P_{13}C_7$ through rapid quenching from the liquid state was firstly obtained by Duwez in 1960s [9]. In general, they are mostly characterized as "single principal element" or "double principal elements" system, for instance, Fe-based, Co-based, Al-based, ZrCu-based amorphous alloys, among others [10-13]. In recent years, multi-principal element amorphous alloys (MPEAAs) are also developed and put forward, which simultaneously own the "multi-principal element" compositional characteristics of medium/high entropy alloys and the structural characteristics of metallic glasses, i.e., long-term disordered and short-term ordered internal atomic arrangement without grain boundary defects and dislocation [14, 15].

Microdevices and information storage put increasing demands on the functions and properties of magnetic materials with the advance of science, technology, and electronic information [16]. The materials applied in different magnetic devices must have good comprehensive features or prominent multiple functional properties, such as good mechanical properties, excellent thermal stability, prominent corrosion resistance, and good magnetic properties. Corrosion is a natural phenomenon that occurs owing to electrochemical or chemical reactions between metals and aggressive corrosive mediums. Hence, it is vital for amorphous alloys to improve their corrosion resistance and high-temperature service stability on the premise of maintaining their good soft magnetic properties.

Qi et al. [17] fabricated a novel series of quinary MPEAAs, namely, $Fe_{25}Co_{25}Ni_{25}(B, Si)_{25}$ metallic glasses with different Si/B ratios. They found the $Fe_{25}Co_{25}Ni_{25}(Si_{0.3}B_{0.7})_{25}$ glassy alloy rods with a diameter of 1.5 mm possessed wide supercooled liquid region (ΔT_x=40 K) and high yield strength of ~3,624 MPa with plastic strain of ~1.7%. Besides, it also has outstanding soft magnetic properties, that is, rather high magnetic flux density (B_s) of ~0.87 T and low coercivity (H_c) of ~1.1 A·m^{-1}. Li et al. [18] also made FeNiCrMo(P, C, B) high entropy metallic glasses (HE-MGs) through copper mold casting method and single-roller melt spinning. They discovered these HE-MGs had a larger supercooled liquid regions of ~69 K, a higher onset crystallization temperatures (T_x) of ~852 K, and a larger undercooling of ~109 K. These alloys presented ultrahigh strength of ~3.4 GPa and Vickers microhardness of ~1,107 HV. Zhang et al. [19] fabricated the senary Fe-Co-Ni-Si-B-Al multi-principal element amorphous ribbons (abbreviated as MPEA ribbons, hereafter) and studied their properties. They pointed out that proper addition of Al could enhance corrosion resistance, but it was harmful to the soft magnetic properties and thermal stability of MPEA ribbons. The self-corrosion current density of these alloy ribbons in 3.5wt.% NaCl solution can maintain the order of 10^{-6} A·cm^{-2}. Wang et al. [20] researched the Mn content on crystallization behaviors and magnetic properties of FeCoNiBMn high entropy amorphous alloys. These MPEA ribbons have an acceptable thermodynamic stability with onset crystallization temperatures in the range of 683–802 K. The B_s of the as-received ribbons ranges from 0.68 T to 0.82 T and all alloy ribbons show very low H_c of less than 1.5 A·m^{-1}. What's more, rare-earth element based, TiZrCu-based, TiZrHf-based, and AlNi-based MPEAAs have been developed and fabricated in recent decades [21-25].

Corrosion resistance is always viewed as a fundamental characteristics of metal materials. Alloying seems to be an effective way that can be adopted to boost the corrosion resistance of amorphous alloys in practical applications [26, 27]. As is known to all, Cr is a corrosion-resistant element with a small atomic radius. Addition of Cr is beneficial for improving anti-corrosion performance without significantly reducing the B_s of the alloys [28]. Shen et al. [29] found that the substitution of a small amount of Fe with Cr could enhance the glass-forming ability (GFA) and the corrosion resistance of Fe-based bulk amorphous alloys in 3wt.% NaCl solutions. Xu et al. [30] prepared $Fe_{79.5-x}Si_{9.5}B_{11}Cr_x$ (x=0, 1, 2, 3, 4, 5, 7, 9, and 11, at.%) metallic glass ribbons via melt spinning method and investigated the effects of Cr addition on thermal stability, soft magnetic properties and corrosion resistance of FeSiB amorphous alloys. They reckoned minor Cr addition significantly improved the corrosion resistance of the FeSiB amorphous alloys. The thermal stability and soft magnetic properties of amorphous alloys have been improved as well. The coercivity of alloy ribbons was decreased from 2.46 A·m^{-1} to 1.47 A·m^{-1} by Cr element addition. Based on laser selective melting technology, Sun et al. [31] prepared $CoCr_xFeMnNi$ high entropy alloys (x=0.4, 0.7, 1.0, 1.3, at.%) and found the strength, plasticity, microhardness, and corrosion resistance can be enhanced by increasing Cr content. The tensile strength and elongation of $CoCr_{1.3}FeMnNi$ high entropy alloys increased to 691 MPa and 18.9%, respectively. Moreover, it has the highest polarization resistance value, the most positive corrosion potential and the lowest corrosion current in 3.5wt.% NaCl solution. Heidari et al. [32] fabricated the $Ti_{0.5}Mo_{0.5}CoNiMnCr_x$ (x=0.5, 1, and 1.5) high entropy alloy thin films by direct current magnetron sputtering. They considered the addition of Cr content could enhance the resistance to general and pitting corrosion. They also deemed that high entropy alloy thin films exhibited superior corrosion resistance in 1 M NaCl compared to the 316L stainless steel substrate.

In some previous studies, the researchers usually pay more attention to the element content change or the addition of a certain element as well as heat treatment on microstructure, thermal stability, magnetic and mechanical properties of MPEAAs [33-36]. There is limited published information regarding the corrosion behavior of multi-principal element amorphous soft magnetic alloys. Therefore, herein, the effects of Cr element doping on the microstructure and physical-chemical properties of FeCoNiSiB multi-principal element alloy in as-spun state were investigated systematacially.

2 Materials and methods

The ingots with nominal compositions of $[Fe_{1/4}Co_{1/4}Ni_{1/4}(Si_{0.3}B_{0.7})_{1/4}]_{100-x}Cr_x$ (x=1, 2, 3, 5, and 8, at.%, aliased as Cr_1, Cr_2, Cr_3, Cr_5, and Cr_8 hereafter) alloys were fabricated by

arc melting a mixture of raw metal materials with purity higher than 99.90wt.% under a Ti-gettered high-purity argon atmosphere. All ingots were re-melted at least five times to ensure chemical homogeneity. As-spun amorphous ribbons with thickness of ~35 μm and width of ~1.3 mm were made by the melt-spinning technique with the linear velocity of ~38 $m \cdot s^{-1}$. The structure of the as-received specimens was examined using an X-ray diffractometer (XRD, Rigaku Smartlab 9KW, Cu-Kα radiation) with a scanning rate of $2° \cdot min^{-1}$ and a high resolution transmission electron microscopy (HRTEM, FEI Tecnai TalosF20) with an accelerating voltage of 200 kV. The surface morphology and surface roughness of the as-received and corroded MPEA ribbons were observed with a scanning electron microscope (SEM, ZEISS GeminiSEM 300) and the non-contact mode of the atomic force microscope (AFM, Brucker Icon) via a scanning area of 10 μm×10 μm. The surface roughness parameters were gained using NanoScope Analysis version 1.7. The thermal properties of Fe-Co-Ni-Si-B-Cr MPEA ribbons were measured using a differential scanning calorimeter (DSC, Netzsch 404F3) with different heating rates under a high-purity Ar atmosphere. Thermal analysis curves can determine the values of T_g (the glass transition temperature), T_x and ΔT_x, and peak crystallization temperatures T_{p1} and T_{p2}. The magnetic parameters including B_s and H_c were measured using a vibrating sample magnetometer (VSM, Lake Shore 7410) under an applied field of 800 $kA \cdot m^{-1}$ and a DC B-H hysteresis loop tracer (Linkjoin MATS-2010SD), respectively. The practical density of the alloys was measured by the Archimedes approach. Microhardness measurements of each specimen were performed using a Vickers semiautomatic hardness tester (HVS-1000A, China). The applied load was 4.90 N for 10 s. Each specimen was measured at seven points, and the average value was calculated as the final microhardness. An electrochemical workstation (CHI660E, China) was used to test the electrochemical properties of the MPEA ribbons with an area of 0.1 cm^2 in 3.5wt.% NaCl solution. A standard three-electrode system consists of a platinum sheet as the counter electrode, a saturated calomel electrode (SCE) as the reference electrode, and the specimen as the working electrode. Before the tests, open circuit potential (OCP) was monitored until it can reach a steady state. Next, the electrochemical impedance spectra (EIS) were conducted under OCP condition, where the frequency ranged from 10^5 Hz to 10^{-1} Hz with an amplitude of 10 mV. The ZsimpWin software was adopted to attain the equivalent circuit and fit the EIS data. Finally, the potentiodynamic polarization tests were tested at a scan rate of $2 mV \cdot s^{-1}$. The electrochemical corrosion parameters, such as self-corrosion potential (E_{corr}), pitting potential (E_{pit}), polarization resistance (R_p), the width of passive region ($\Delta E = E_{pit} - E_{corr}$), corrosion current density (I_{corr}), and passive current density (I_{pass}), were obtained via fitting the polarization curves. To confirm the reliability of data, the potentiodynamic polarization and EIS tests were recorded after triplicate measurements. Meanwhile, the corroded microstructure of all ribbon samples was observed after immersing in 3.5wt.% NaCl solution for 100 h.

3 Results and discussion

3.1 Structure of the MPEA ribbons

Thermodynamic parameters, such as the entropy of mixing (ΔS_{mix}), the enthalpy of mixing (ΔH_{mix}), the average atomic radius difference (δ), valence electron concentration (VEC), and comprehensive thermodynamic parameter (Ω), are often directly used to predict the phase formation of MPEAs before the preparation [37, 38]. As a rule, an amorphous nature is formed in MPEAs when $9\% \leq \delta \leq 18.5\%$, $-49 kJ \cdot mol^{-1} \leq \Delta H_{mix} \leq -8 kJ \cdot mol^{-1}$, $7 J \cdot (mol \cdot K)^{-1} \leq \Delta S_{mix} \leq 16 J \cdot (mol \cdot K)^{-1}$, and $\Omega \geq 1.1$ [39]. Table 1 shows the calculated thermodynamic parameters of alloy ribbons with different Cr content. From Table 1, it can be seen these parameters meet the requirements of glassy structure formation of MPEAs on the whole. Figure 1(a) exhibits the typical XRD patterns of Fe-Co-Ni-Si-B-Cr alloy ribbons in as-spun state. It can be seen that all of alloy ribbons present a broad single diffuse peak, and no distinctly sharp diffraction peaks corresponding to crystalline phases are visible, which indicates these ribbons have the characteristics of amorphous phases. In order to verify the glassy nature of MPEA ribbons, the Cr_3 specimen was selected as a representative to achieve an in-depth examination of the microstructure by high-resolution transmission electron microscopy (HRTEM). Figure 1(b) shows the HRTEM image along with corresponding selected area electron diffraction (SAED) pattern of the melt-spun Cr_3 sample. A full diffuse halo ring without any detectable crystalline diffraction spots can be observed in the SAED pattern. Cr_3 specimen exhibits the glassy structure of maze-like patterns without any lattice fringe in the HRTEM image, further confirming the absence of crystalline phase or crystal-like regions.

Figure 2 shows secondary electron images of the surface morphology of these rapid-solidified MPEA ribbons with various Cr content. As expected, the microstructure of these alloy ribbons is rather uniform and the surface is also flawless, especially no visible coarse grains and dendritic crystals on the surface. Besides, scarcely any residual porosities and gaps can be observed. The above-mentioned findings agree well with the experimental results from its XRD patterns. This is chiefly because the melt-spinning approach can impede the grain formation by virtue of the high cooling rates ($\sim 10^6 K \cdot s^{-1}$) [40].

Table 1: Calculated thermodynamic parameters ΔH_{mix}, ΔS_{mix}, δ, VEC, and Ω for MPEA ribbons with various Cr content

Alloy samples	ΔS_{mix} [$J \cdot (mol \cdot K)^{-1}$]	ΔH_{mix} ($kJ \cdot mol^{-1}$)	δ (%)	VEC	Ω
Cr_1	13.13	−22.90	13.72	7.559	1.093
Cr_2	13.36	−22.88	13.66	7.543	1.114
Cr_3	13.53	−22.86	13.60	7.528	1.131
Cr_5	13.81	−22.80	13.48	7.496	1.159
Cr_8	14.09	−22.69	13.29	7.449	1.193

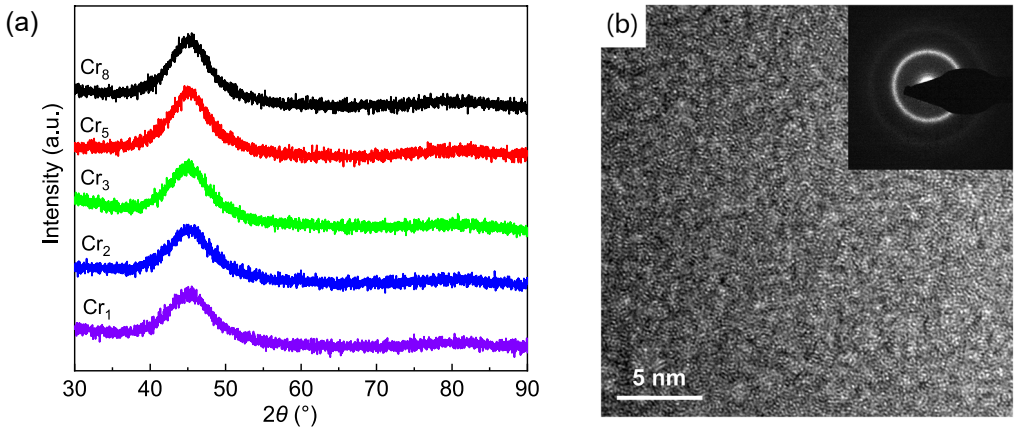

Fig. 1: XRD patterns of $[Fe_{1/4}Co_{1/4}Ni_{1/4}(Si_{0.3}B_{0.7})_{1/4}]_{100-x}Cr_x$ (x=1, 2, 3, 5, 8, at.%) melt-spun alloy ribbons (a), and HRTEM image and the corresponding SAED pattern of Cr_3 specimen (b)

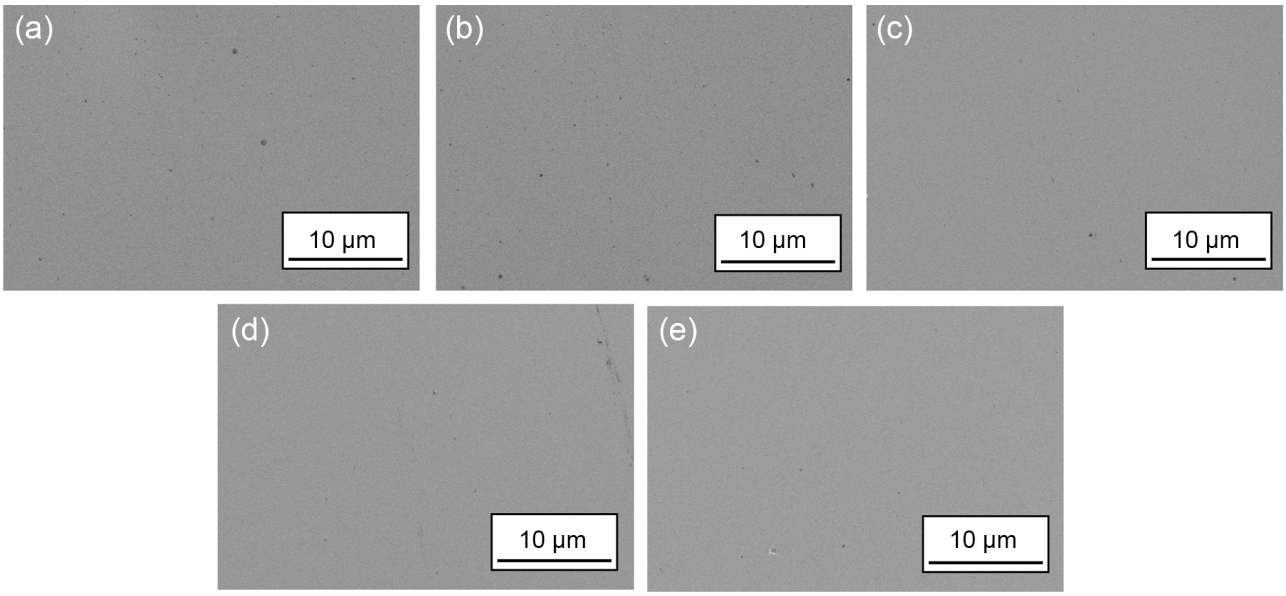

Fig. 2: SEM images of as-spun MPEA ribbons: (a) Cr_1; (b) Cr_2; (c) Cr_3; (d) Cr_5; (e) Cr_8

Figure 3 shows the typical two-dimensional surface morphologies of these glassy alloy ribbons. These images present a smooth feature, implying the amorphous nature of all MPEA ribbons. As can be seen from Figs. 3(b) and (c), some visible white spots are observed due to the fact that some magnetic contaminations are absorbed on the alloy ribbon surface [41]. The surface characteristics are also reflected in the average protrusion height and roughness values of the ribbon surface. Table 2 lists the surface topographical parameters containing the Z scale, ten-point mean roughness (R_z), root mean square roughness (R_q), and average roughness (R_a). Z scale implies the difference of peak and valley in height values within the analyzed area. The meanings and calculated equations of the other three parameters can be referred to the Ref. [42]. From Table 2, the values of R_q maintain 0.562 nm or below and the Cr_2 and Cr_3 samples own the relatively higher values compared with the others. The values of R_a of the MPEA ribbons are ranged of 0.180–0.306 nm, suggesting that Cr addition has a mild influence on the roughness. The alloy composition is vital to their microstructure and the properties. Cr element is one of the commonly-used elements in FeCoNi-based amorphous alloys or FeCoNi-containing high entropy alloys. Meanwhile, Cr element has similar atomic radius with the other three elements. Thus, the addition of Cr does not affect the roughness of the previous FeCoNi-based alloys. Besides, the linear speed of melt-spinning approach is about 38 $m \cdot s^{-1}$ as described above, and the alloy ribbons present amorphous nature according to XRD patterns. Hence, it can be concluded that the roughness of MPEA ribbons varies slightly and is probably not a significant influencing factor in our subsequent performance study.

3.2 Thermal analysis of the MPEA ribbons

The non-isothermal DSC curves presented in Fig. 4(a) show the crystallization behavior of these Cr-containing glassy ribbons. The thermal parameters, including T_g, T_x, T_{p1}, T_{p2}, and ΔT_x are listed in Table 3. It is known from Fig. 4 and Table 3 that the thermal stability of MPEA ribbons decreases gradually with the addition of Cr element. With the increase of Cr element, the values of T_g and T_x decrease from 782.0 K

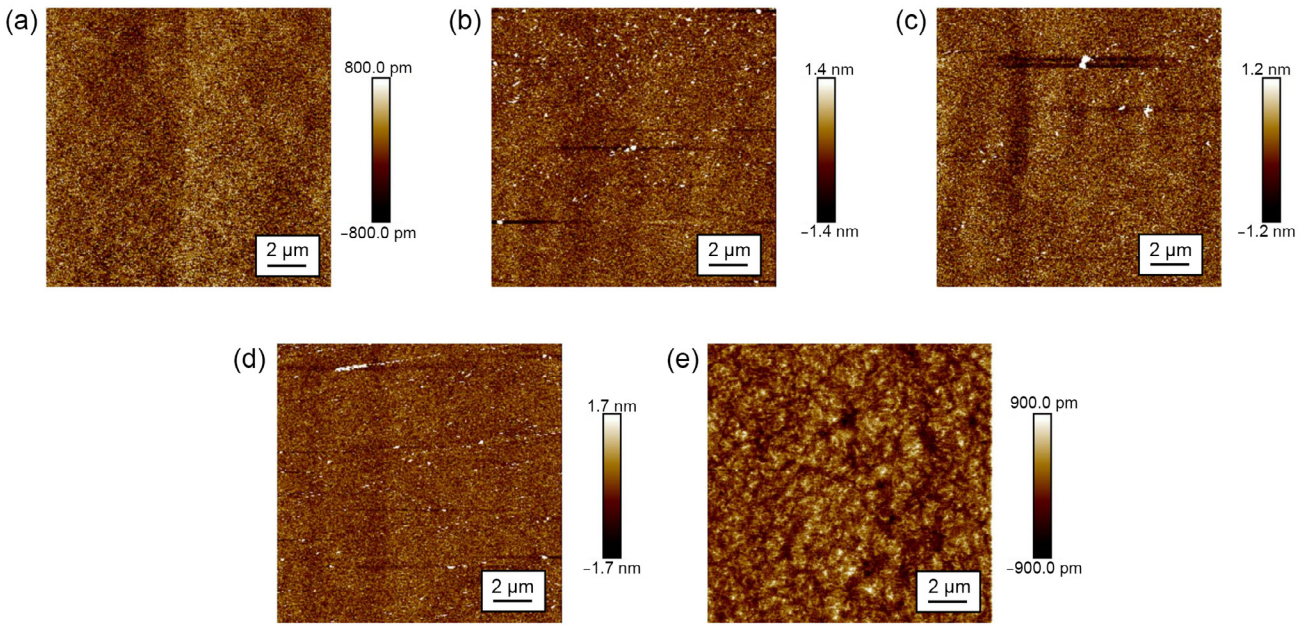

Fig. 3: Two-dimensional AFM images of as-spun MPEA ribbons: (a) Cr_1; (b) Cr_2; (c) Cr_3; (d) Cr_5; (e) Cr_8

Table 2: AFM surface characteristics of as-spun MPEA ribbons

Alloys samples	*Z* scale (nm)	Ten-point mean roughness, R_z (nm)	Root mean square roughness, R_q (nm)	Average roughness, R_a (nm)
Cr_1	4.7	0.499	0.240	0.190
Cr_2	25.1	0.919	0.562	0.306
Cr_3	19.8	0.794	0.552	0.295
Cr_5	23.5	0.993	0.502	0.299
Cr_8	12.6	0.285	0.341	0.180

and 821.5 K for Cr_1 sample to 749.0 K and 781.5 K for Cr_8 sample, respectively. In addition, the value of ΔT_x usually could be employed as a posterior indicator to evaluate the GFA of amorphous alloys [43]. The width of supercooled liquid region increases firstly and then decreases. In the meantime, the Cr_2 specimen owns the maximum value (~43.5 K) of ΔT_x, which means it has the highest GFA among the investigated MPEA ribbons. Furthermore, it is worth noting that another faint peak is generated from the left side of main exothermic peak when the content of Cr exceeds 5at.%, indicating that there might be some complicated multi-stage crystallization processes. The non-isothermal DSC traces of Cr_1 specimen obtained at different heating rates are shown in Fig. 4(b). All the DSC curves exhibit a single exothermic peak, and the onset crystallization signals for Cr_1 sample under the different heating rates are marked by arrows in the scans. As the heating rate increases, all characteristic temperatures apparently move towards higher values and the exothermic peaks become more acute, implying that the crystallization behavior of Cr_1 ribbons is influenced by heating rates and exhibits an obvious thermodynamic effect [44]. In order to further explore the crystallization kinetics of Cr_1 specimen, the volume fraction of the crystalline phases (α) as a function of temperature (T) has been obtained from the DSC curves. The α can be calculated according to the Refs. [45, 46]. The dependence of the α on the temperature is plotted in Fig. 4(c). According to Fig. 4(c), crystallization at higher heating rates takes place at higher temperatures, and vice versa. Under different heating rates, the shapes of all curves are almost similar and present typical sigmoid shape ("S" type), each "S" can be divided into three stages. As to a certain heating rate, the curves of incipient and terminal stages (α<0.1 and α>0.9) are gentle, which are corresponding to the grain nucleation process of the crystallization and the almost-completed crystallization process [47, 48]. By contrast, the middle stage (0.1<α<0.9) is steep, which means the crystallized reaction occurs stably at this stage. That is to say, the nucleation and growth of the crystalline nucleus contribute to crystallization [49]. With the increase of the heating rates, the curves of α vs T shift to the higher temperature regions and the crystallization rate α/T decreases, which shows that the crystallization of Cr_1 ribbons has obvious kinetics effect. The dependence of the crystallization rate on heating rate can be ascribed to the thermally activated processes of crystallization [50].

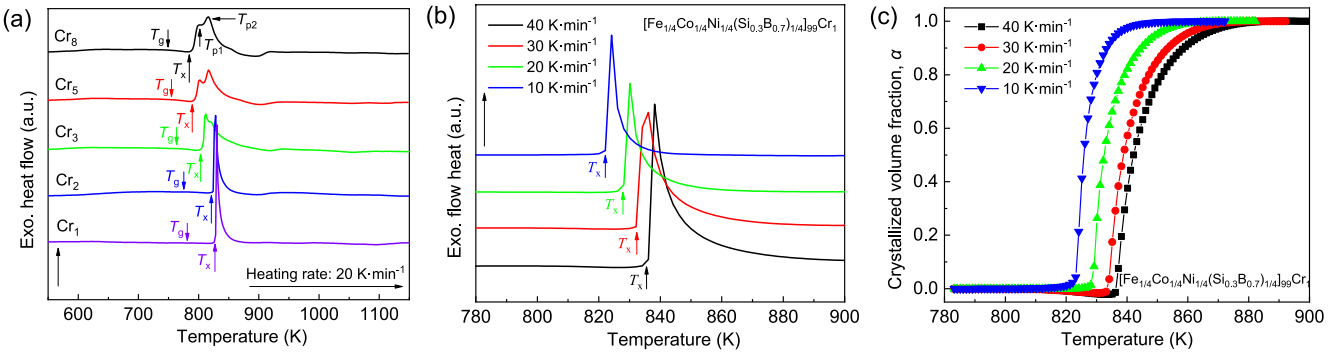

Fig. 4: DSC curves of as-spun MPEA ribbons at a heating rate of 20 K·min^{-1} (a), DSC curves of Cr_1 specimen under various heating rates (b), and curves of α vs T of Cr_1 specimen under different heating rates (c)

Table 3: Thermal parameters under non-isothermal crystallization with a heating rate of 20 K·min^{-1} for MPEA ribbons containing various Cr content. The error is no more than ±2 K

Alloy samples	T_g (K)	T_x (K)	ΔT_x (K)	T_{p1} (K)	T_{p2} (K)
Cr_1	782.0	821.5	39.5	829.0	–
Cr_2	776.0	818.5	43.5	826.0	–
Cr_3	764.5	801.0	36.5	811.0	–
Cr_5	755.0	786.0	31.0	802.0	817.5
Cr_8	749.0	781.5	32.5	801.0	816.0

3.3 Soft magnetic properties and microhardness of the MPEA ribbons

Figure 5(a) shows the hysteresis loops of the as-spun MPEA ribbons with excellent magnetic softness at ambient temperature. All of the ribbons exhibit a typical soft magnetic hysteresis characteristic, i.e., a tendency for very fast saturation with a magnetic field increment due to their negligible demagnetizing effect [51]. The corresponding B_s and H_c variation tendency of ribbon samples is depicted in Fig. 5(b). From Fig. 5, it can be concluded that the B_s of the MPEA ribbons shows a non-linear variation tendency as the Cr increases and the values are in the range of 0.427–0.578 T. The largest B_s value is approximately 0.578 T for Cr_3 specimen, which is a little bit higher than those of $(Co_{0.6}Fe_{0.3}Ni_{0.1})_{66}(B_{0.811}Si_{0.189})_{29}Nb_5$ and $(Co_{0.8}Fe_{0.2})_{67.5}Gd_{3.5}Nb_4B_{25}$ multi-component metallic glasses [52, 53]. At the same time, Cr_3 ribbons also have the relatively small coercive force (~5.5 A·m^{-1}), which is sightly lower than that of $Fe_{25}Co_{25}Ni_{25}(P_{0.2}C_{0.6}B_{0.2})_{25}$ HE-MGs (~6.4 A·m^{-1}) and much lower than those of the ferromagnetic HEAs, such as CoCrFeNiCuAl, CoCrFeNiTiAl, and $FeCoNi(AlSi)_{0.8}$ [54-56]. The small H_c values of MPEA ribbons spanning from 4.6 A·m^{-1} to 8.5 A·m^{-1} can be originated from the homogeneous amorphous structure with low magnetocrystalline anisotropy in the absence of any nuclei or clusters [57, 58].

Figure 6 indicates the hardness results of melt-spun MPEA ribbons. It can be inferred from this diagram that the microhardness of MPEA ribbons reduces overall with an increasing Cr content. Cr_1 sample owns the largest microhardness at 1,133 $HV_{0.5}$, which is roughly close to the value of large-size $Fe_{71}Ni_9P_{12}B_{4.9}Si_{2.5}Cu_{0.6}$ amorphous ultra-thick ribbons by twin-roll strip casting and is also a little higher than those of $FeNiCrMo(P_{0.6}C_{0.2}B_{0.2})_{20}$ and $Fe_{68.5}Si_{18.5}Cu_1Nb_3B_9$ MPEA ribbons [18, 59-61]. The values of all MPEA ribbons are more than 810 $HV_{0.5}$, which is also twice as much as the hardness of CoCrCuFeNiV HEAs (~408.4 $HV_{0.2}$), demonstrating their outstanding friction and wear performance [62]. High microhardness can be attributed to the cocktail effect of HEAs in performance, especially for physical and mechanical properties [63, 64]. Additionally, boron and silicon elements, as the small-sized non-metal elements in Fe-Co-Ni-Si-B-Cr alloy system, can fill the interstitial sites of MPEA ribbons, leading to a denser structure of the alloy ribbons and resulting in a solid solution strengthening effect [41, 65, 66].

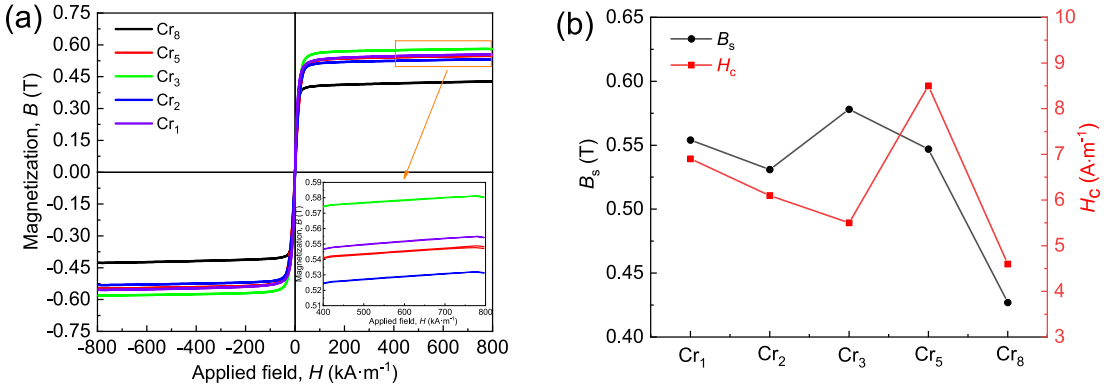

Fig. 5: Hysteresis loops (a) and variation tendency of B_s and H_c with Cr content (b) of melt-spun MPEA ribbons

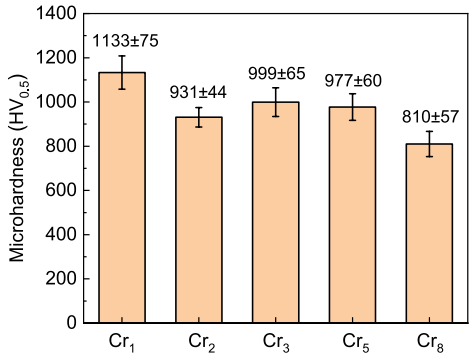

Fig. 6: Vickers microhardness of melt-spun MPEA ribbons

3.4 Corrosion resistance and immersion tests of the MPEA ribbons

Figure 7 reveals the electrochemical corrosion behavior of MPEA ribbons in 3.5wt.% NaCl solution. Figure 7(a) shows the potentiodynamic polarization curves of MPEA ribbons with various Cr content. As can be seen from Fig. 7(a), in the process of anodic polarization, the MPEA ribbons undergo a dynamic transition of activation and passivation after passing the Tafel region. A rather stable passive film forms when Cr content reaches 8at.%. Whereafter, the current density is suddenly enhanced when the voltage increases to a certain value, suggesting the occurrence of pitting corrosion. E_{pit} is usually defined as the potential at which the current density has a sharp rise. I_{pass} means the current density, which changes little when potential increases and can be obtained from the potentiodynamic polarization curve near the middle of the passivation zone [67]. Table 4 summarizes the electrochemical corrosion parameters of MPEA ribbons estimated from polarization curves by the Tafel extrapolation method. I_{corr} and E_{corr} are connected with the actual corrosion rate and corrosion tendency, respectively. In general, a higher corrosion potential, a larger polarization resistance, and a smaller corrosion current density infer that the metal materials possess superior corrosion resistance [68, 69]. Thus, the general corrosion resistance of the MPEA ribbons in the 3.5wt.% NaCl solution follows the order, from high to low: Cr_8>Cr_5>Cr_3>Cr_1>Cr_2. Besides, increasing the Cr content does not result in obvious difference in I_{corr} and I_{pass} of the five alloys because they still maintains the same order of magnitudes, but causes a noticeable variation in E_{pit} and ΔE. To be specific, the addition of Cr leads to an increase in the E_{pit} and ΔE owing to the wider passivation region, and the values of E_{corr}, I_{corr}, and I_{pass} are in the range of −0.340–−0.411 V, 2.061–4.288 μA·cm^{-2}, and 6.807–11.220 μA·cm^{-2}, respectively. Cr_8 sample owns the highest E_{corr} of −0.340 V, the largest ΔE of 0.628 V, and the most positive E_{pit} of 0.288 V, implying it has the best passivation film stability compared to the other four Cr-containing MPEA ribbons in this study. In contrast, for the Cr_1 ribbons, the polarization curve manifests the most narrow passive region (ΔE=0.263 V) with the most negative E_{pit} value of −0.130 V and a relative high I_{corr} value of 3.267 μA·cm^{-2}. Therefore, it can be concluded that the pitting corrosion resistances of MPEA ribbons improve with an increase in Cr content in this alloy system. However, it is also worth noting that the Cr_8 alloy exhibits the largest I_{pass} value of 11.220 μA·cm^{-2}, suggesting its passivation film might be more

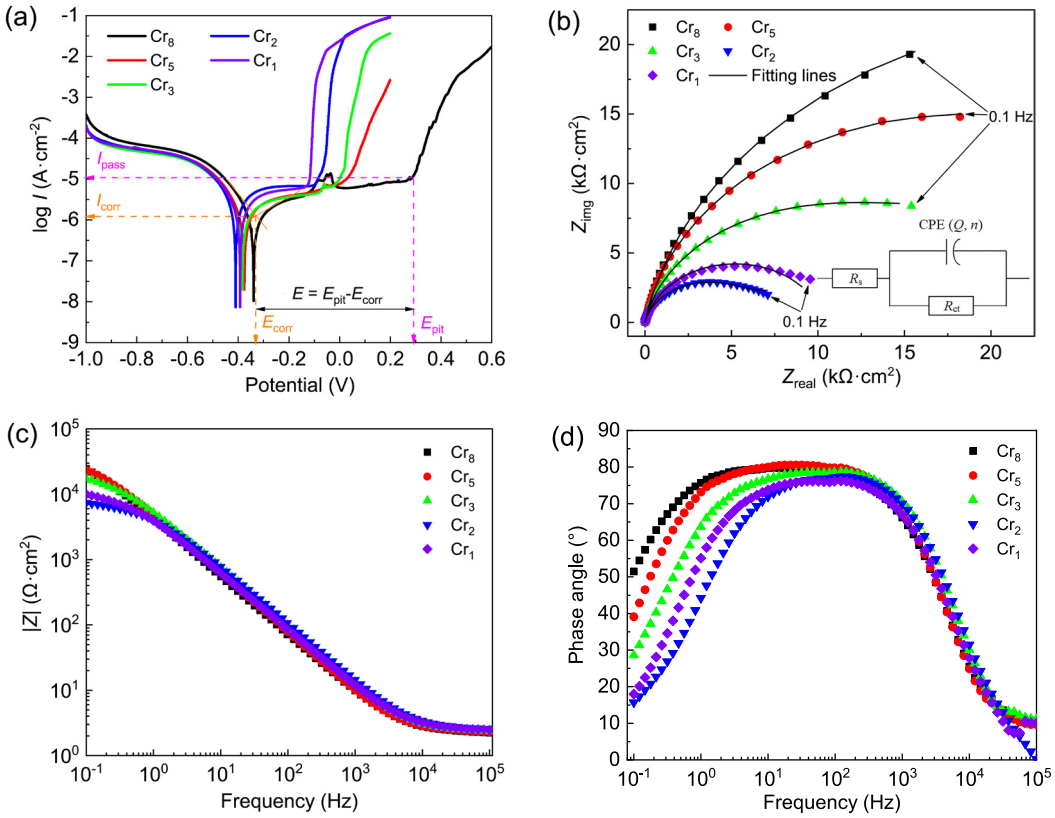

Fig. 7: Potentiodynamic polarization curves of as-spun MPEA ribbons in a 3wt.% NaCl solution (a), Nyquist plots (b), Bode modulus plots (c), and Bode phase angle plots of MPEA ribbons in a 3.5wt.% NaCl solution (d)

Table 4: Electrochemical corrosion kinetic data estimated from polarization curves of MPEA ribbons and some typical metal materials in a 3.5wt.% NaCl solution

Alloy samples	E_{corr} (V)	I_{corr} (μA·cm^{-2})	R_p (kΩ·cm^2)	E_{pit} (V)	I_{pass} (μA·cm^{-2})	ΔE (V)	Ref.
Cr_1	−0.393	3.267	14.00	−0.130	6.808	0.263	This work
Cr_2	−0.411	4.288	11.01	−0.096	7.691	0.315	
Cr_3	−0.384	2.061	21.28	−0.025	6.807	0.359	
Cr_5	−0.377	2.200	19.84	0.017	9.057	0.394	
Cr_8	−0.340	2.076	19.82	0.288	11.220	0.628	
Permalloy ribbons	−0.420	800.000	–	–	–	–	[75]
$FeCoNiCuAlCe_{0.03}$ HEAs	−0.430	4.610	–	-0.170	–	0.260	[75]
$Fe_{82}Cr_2Nb_1B_8P_4Si_2C_1$ MGs	−0.422	4.060	–	-0.027	–	0.395	[76]
316L stainless steel	−0.622	48.040	–	0.471	–	1.093	[77]
310 stainless steel	−0.310	1.360	19.12	–	–	–	[78]

loose compared to the ribbons with 5at.% Cr or below. For comparison, the corrosion parameters of some typical metal materials are also listed in Table 4. It can be shown that except for Cr_1 and Cr_2 samples, the I_{corr} of the other MPEA ribbons is smaller than that of HEAs, MGs, 316L stainless steel, and traditional soft magnetic alloys, but is slightly higher than that of 310 stainless steel. This indicates that the corrosion resistance of MPEA ribbons is better than the other four metal materials and is comparable to 310 stainless steel [75-78]. However, as for pitting corrosion, 316L stainless steel exhibits a more positive E_{pit} and a larger ΔE, which means the pitting corrosion resistance of MPEA ribbons is poorer than that of 316L stainless steel.

To gain a detailed understanding of the electrochemical processes dissimilarities taking place on the surface of the MPEA ribbons, the electrochemical impedance spectra was carried out. Figures 7(b)–(d) depict the Nyquist and Bode diagrams for the five kinds of MPEA ribbons at OCP. The Nyquist plots exhibit one capacitance arc caused by the dispersion effect and without inductive arcs, indicating merely one time constant could be detected and there exists a charge-transfer process [70, 71]. By and large, the radius of the capacitance arc increases with the Cr addition. The diameter of the capacitive semicircles in the Nyquist plots for Cr_8 is the largest, suggesting that the Cr_8 alloy has the best resistance to chloridion erosion. Meanwhile, the impedance modulus at low frequencies, such as $|Z|_{0.01\ Hz}$ or $|Z|_{0.1\ Hz}$, is also commonly utilized as a semi-quantitative indicator of corrosion resistance and reflects the minimum degree of ion penetration [67, 72]. The value of $|Z|_{0.1\ Hz}$ decreases in the order of Cr_8, Cr_5, Cr_3, Cr_1 and Cr_2 samples. Generally, the $|Z|$ value is also applied to characterize the polarization resistance [73]. In Fig. 7(c), the $|Z|$ values of the as-spun MPEA ribbons from the largest to the smallest are as follows: Cr_8, Cr_5, Cr_3, Cr_1, Cr_2 samples. The Cr_8 ribbons has the largest modulus of 24,700 Ω·cm^2, while the Cr_2 ribbons has the smallest modulus of 7,360 Ω·cm^2. The curves of phase angle for MPEA ribbons in Fig. 7(d) exhibit similar shape, which increases from around 0° or 10° in the high frequency of 10^5 Hz, followed by the highest phase angles near 80° in the middle frequency ranged from 10–10^3 Hz, and to about 15° for Cr_1 and Cr_2 ribbons and 50° for Cr_8 ribbons in the low frequency of 10^{-1} Hz. Cr_8 alloy exhibits the largest phase angle and maintains a maximum plateau over a wider frequency range. By contrast, Cr_1 and Cr_2 alloys own the lowest phase angle in the low-frequency range, which is trait of high-capacitance materials, hinting that the increase in charge accumulation on the ribbon surface expedites corrosion process [74]. These results further suggest that both the chemical stability of the passive film and pitting-resistant ability of alloys improve with increasing Cr content.

The EIS data were fitted by an equivalent circuit $[R_s(QR_{ct})]$ presented in the inset of Fig. 7(b). In this inset, R_s and R_{ct} denote the solution resistance and charge transfer resistance at the metal/solution interface. The radius of a curve in a Nyquist plot is related to R_{ct}. A larger curve radius represents a larger R_{ct}, indicating strong corrosion resistance of the specimen. Moreover, a constant phase element (CPE) of the capacitance of the electrical double layer is employed to replace the pure capacitance to indicate the non-ideal capacitance behavior caused by a variety of factors like the surface inhomogeneity, the roughness, and the electrode porosity on the metal surface. The impedance of CPE is expressed as follows:

$$\mathrm{CPE} = Q^{-1}(j\omega)^{-n} \quad (1)$$

where j is the imaginary number, ω is the angular frequency, Q is the admittance magnitude of the CPE, and n means dispersion coefficient, which is the value for the deviation between the system and the ideal capacitance behavior with a range from 0 to 1. The n with the values of 1, 0.5, and 0 refers to ideal capacitance, Warburg impedance, and a pure resistor,

respectively. The fitting parameters of the equivalent circuit, including R_s, R_{ct}, CPE, n, and chi-square values (χ^2), are summarized in Table 5. From Table 5, it can be seen the values of R_s, which is frequently regarded as a concentration indicator of corrosion products near the electrode surface, exhibit a marginally diminishing trend, meaning the corrosion products are dissolved in the corrosive media [79]. The small chi-square values in the 10^{-4} order of magnitudes indicate that the adopted equivalent circuit model shows the well-fitting results and suitably characterizes the corrosion behaviors of alloys. The R_{ct} value of the Cr_8 sample (~47.19 kΩ·cm^2) is obviously higher than those of the other studied specimens, implying its competitive corrosion properties among the proposed MPEA ribbons. Furthermore, CPE often reflects the defect degree of the passive films [80]. Thus, the change in the CPE values indicates that the passive film of the MPEA ribbons with 8at.% Cr is the most stable compared with that of the others one. Overall, the fitting data by EIS measurements is in agreement well with the experimental results of potentiodynamic polarization curves.

Figure 8 shows the corrosion morphology of the MPEA ribbons after immersing in a 3.5wt.% NaCl solution for 100 h. The corrosion morphology of the Cr_1 and Cr_2 alloys shows obvious residual salt particles deposited on the ribbon surface, which is in accordance with our previous research regarding FeCoNi-containing high entropy amorphous alloy ribbons [19]. On the contrary, there is not visible corrosion products adhered to the surface of Cr_8 ribbons, indicating its superior corrosion resistance against chloride ion. These experimental pictures are also consistent with the results of potentiodynamic polarization curves. In summary, the above-mentioned results indicate that the MPEA ribbons synthesized in this study possess excellent corrosion resistance. This can be attributed to the addition of corrosion-resistant Cr element as well as the chemical and structural homogeneity of these MPEA ribbons [81].

Table 5: Fitting electrical parameters for MPEA ribbons in 3.5wt.% NaCl solution

Alloy samples	R_s (Ω·cm^2)	CPE (Ω·s^n·cm^{-2})	n	R_{ct} (kΩ·cm^2)	χ^2 (×10^{-4})
Cr_1	2.466	3.314×10^{-5}	0.8679	10.40	7.786
Cr_2	2.550	3.247×10^{-5}	0.8813	6.33	4.716
Cr_3	2.371	3.470×10^{-5}	0.8912	17.05	8.504
Cr_5	2.364	3.727×10^{-5}	0.9060	30.96	9.446
Cr_8	2.262	4.591×10^{-5}	0.8878	47.19	9.912

4 Conclusions and prospects

In this work, a series of senary Fe-Co-Ni-Si-B-Cr multi-principal element amorphous alloys were successfully fabricated by single-roller melt-spinning approach. The microstructure, thermal stability, microhardness, soft magnetic, and anti-corrosion properties of as-spun MPEA ribbons were investigated in detail. The main research findings can be summarized as follows:

(1) $[Fe_{1/4}Co_{1/4}Ni_{1/4}(Si_{0.3}B_{0.7})_{1/4}]_{100-x}Cr_x$ (x=1, 2, 3, 5, 8, at.%) senary alloy ribbons own the fully glassy structure and exhibit excellent thermal stability with a high onset crystallization temperature of 781.5 K or above. But the thermal stability of MPEA ribbons reduces gradually with the increasing Cr doping in multi-principal element alloy system.

(2) The microhardness values of MPEA ribbons with various Cr content are over 810 $HV_{0.5}$. Besides, these investigated alloy ribbons exhibit a typical soft magnetic hysteresis characteristic and as-spun Cr_3 sample has the largest B_s value of 0.578 T and the relatively small coercivity of ~5.5 A·m^{-1}.

(3) As the Cr content increases, the corrosion resistance of MPEA ribbons becomes superior and exhibits the obvious passive regions in a 3.5wt.% NaCl solution. The electrochemical results show that the Cr_8 sample exhibits the highest self-corrosion

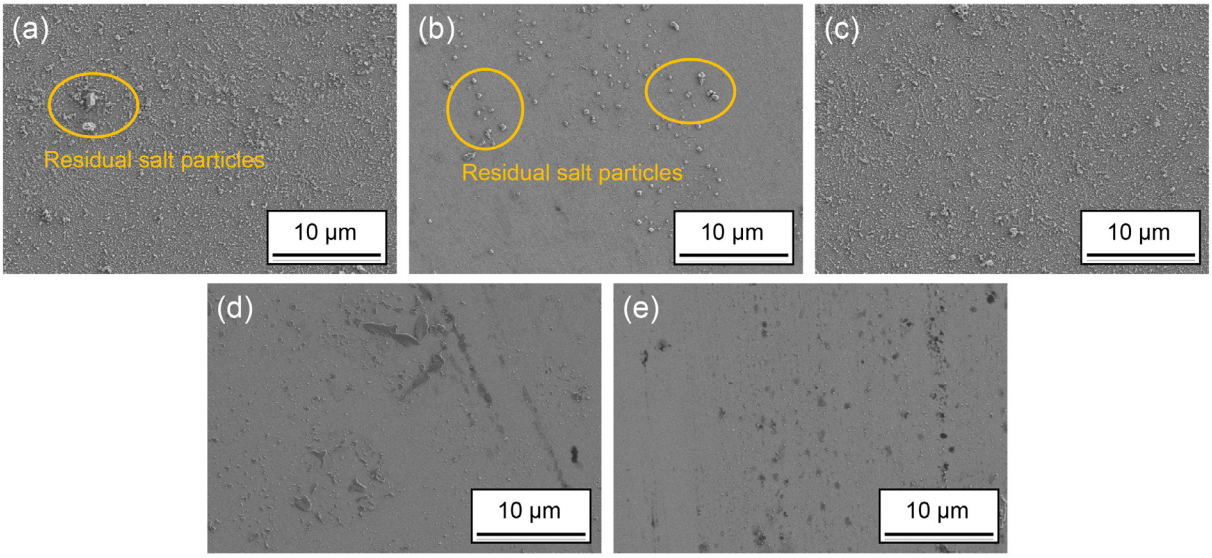

Fig. 8: Surface morphology of MPEA ribbons in a 3.5wt.% NaCl solution for 100 h: (a) Cr_1; (b) Cr_2; (c) Cr_3; (d) Cr_5; (e) Cr_8

potential, a comparatively low corrosion current density, the most positive pitting potential, and the widest passive region among the studied amorphous ribbons.

Considering the above study results, future research work can be centered on the practical engineering application of this cutting-edge and promising alloy materials. In reality, the MPEA ribbons or metallic glass ribbons and gas-atomized amorphous alloy powders have the roughly similar cooling rates. Therefore, it is indeed worthwhile to exploit the chemical composition and preparation technique about high-performance multi-principal element amorphous powders as well as fabricate some multi-principal element amorphous-nanocrystalline alloy coatings by advanced spraying technology to meet the national needs of oceanic, electronics, and mechanical engineering industries. In addition, amorphous-nanocrystalline alloys, particularly those with high permeability, low power loss, and low coercivity, such as Co-based metallic glasses, Fe-based nanocrystalline materials, and FeCo-based soft magnetic alloys, have become the candidates for shielding static magnetic fields and solving the accuracy limitations in measuring ultra-weak magnetic fields. With the continuous improvement of the comprehensive performance requirements for metal materials, the multi-principal element amorphous-nanocrystalline alloys would also be expected to emerge as competitive soft magnetic materials with high permeability, low magnetic noise, and some other excellent all-round performance, so as to overcome the sensitivity limitations faced in extremely-weak magnetic measurements in diverse complex environments in the future.

Acknowledgments

This work was supported by the National Natural Science Foundation of China (Grant Nos. 52401202, 62203028, 52275225). The authors are thankful sincerely to Dr. Jia-wen Sun and Dr. Mei-fang Wang from Shiyanjia Lab (www.shiyanjia.com) for the XRD, AFM and SEM characterizations. The authors are grateful truly to Dr. Xue-fei Qin from eceshi (www.eceshi.com) for the TEM characterization and VSM tests as well.

Conflict of interest

The authors declare that they have no known competing financial interests or personal relationships that could have appeared to influence the work reported in this paper.

References

[1] Han Y, Chen H, Sun Y, et al. Ubiquitous short-range order in multi-principal element alloys. Nature Communications, 2024, 15: 6486.
[2] Yu B, Ren Y, Zeng Y, et al. Recent progress in high-entropy alloys: A focused review of preparation processes and properties. Journal of Materials Research and Technology, 2024, 29: 2689–2719.
[3] Zhu D, Hu S, Fu Y, et al. A review of preparation methods, friction and wear, corrosion, and biocompatibility of biomedical high-entropy alloys. Journal of Materials Science, 2024, 59: 1153–1183.
[4] Krishna S, Noble N, Radhika N, et al. A comprehensive review on advances in high entropy alloys: Fabrication and surface modification methods, properties, applications, and future prospects. Journal of Manufacturing Processes, 2024, 190: 583–606.
[5] Zhao C, Cai W, Sun N, et al. Facile preparation of porous high-entropy alloy FeCoNiCuMn and its OER performance. Journal of Physics and Chemistry of Solids, 2024, 184: 111668.
[6] Ye X, Diao Z, Kang H, et al. A new strategy for the design of triple-phase eutectic high-entropy alloys based on infinite solid solution and pseudo-ternary method. Nano Letters, 2024, 24: 6117–6123.
[7] Hou S, Li C, Li C, et al. Progress in composition design and preparation methods of large amorphous alloys. Chinese Journal of Rare Metals, 2024, 48: 240–253.
[8] Tian L, Li C, Zhai J, et al. Progress in functional research of amorphous alloys. Chinese Journal of Rare Metals, 2021, 45: 998–1009.
[9] Lin S, Duwez P. Structure of an amorphous FePC alloy. Physica Status Solidi, 1969, 34(2): 469–474.
[10] Huo Z, Zhang G, Han J, et al. A review of the preparation, machining performance, and application of Fe-based amorphous alloys. Processes, 2022, 10: 1203.
[11] Li J, Li W. Structure and glass-forming ability of Al-based amorphous alloys. Acta Metallurgica Sinica, 2022, 58: 457–472.
[12] Hu L, Mu C, Ma H, et al. Soft magnetic properties and giant magneto-impedance effect of $Co_{68.15}Fe_{4.35}Si_{12.5}B_{15-x}Cr_x$ amorphous ribbons. Journal of Non-Crystalline Solids, 2023, 608: 122264.
[13] Liang S, Zhu F, Wang Y, et al. On the kinetics of structural evolution in metallic glasses. International Journal of Engineering Sciences, 2024, 205: 104146.
[14] Wang W. High-entropy metallic glasses. JOM, 2014, 66: 2067–2077.
[15] Jiang L, Bao M, Dong Y, et al. Processing, production and anticorrosion behavior of metallic glasses: A critical review. Journal of Non-Crystalline Solids, 2023, 612: 122355.
[16] Yang S, Zhang Z, Xu K, et al. Study on the soft magnetic properties, corrosion, and wear resistance of Ni-Co-W coatings deposited via laser-assisted electrochemical technique: Potential applications in advanced electromagnetic devices. Materials Today Communications, 2024, 40: 109907.
[17] Qi T, Li Y, Takeuchi A, et al. Soft magnetic $Fe_{25}Co_{25}Ni_{25}(B, Si)_{25}$ high entropy bulk metallic glasses. Intermetallics, 2015, 66: 8–12.
[18] Li Y, Wang S, Wang X, et al. New FeNiCrMo(P, C, B) high-entropy bulk metallic glasses with unusual thermal stability and corrosion resistance. Journal of Materials Science & Technology, 2020, 43: 32–39.
[19] Zhang S, Ma D, Liang X, et al. Influence of Al addition on the microstructure and properties of $Fe_{25}Co_{25}Ni_{25}(Si_{0.3}B_{0.7})_{25}$ high entropy metallic glass. Intermetallics, 2024, 169: 108304.
[20] Wang S, Wang F, Liang Y, et al. Effect of Mn content on crystallization behaviors and magnetic properties of FeCoNiBMn high-entropy amorphous alloys. Journal of Materials Research and Technology, 2024, 28: 4754–4763.
[21] Zhang S, Zhang Z, Gao Y, et al. Research progress in high-entropy metallic glasses: Comprehensive properties and composition patterns characteristics. Rare Metal Materials and Engineering, 2021, 50: 2215–2228.

[22] Shi L, Shao Y, Fan Z, et al. Connecting the composition, structure, and magnetic property in high-entropy metallic glasses. Acta Materialia, 2023, 254: 118983.
[23] Zhang S, Zhang Z, Chen C, et al. Relation between quenching wheel speed and microstructure, thermal stability and corrosion resistance of quinary Al-Ni-Y-Co-Si high entropy metallic glass ribbons prepared by melt spinning. Journal of Non-Crystalline Solids, 2023, 601: 122049.
[24] Zhang S, Zhang Z, He P, et al. Effect of Co addition on the microstructure, thermal stability and anti-corrosion properties of $AlNiZrYCo_x$ high-entropy metallic glass ribbons. Journal of Non-Crystalline Solids, 2022, 585: 121555.
[25] Wang Y, Si J, Si Y, et al. Preparation and electrochemical corrosion performances of Zr-Ti-Ni-Cu-Be high-entropy bulk metallic glasses. Materials Science and Engineering: B, 2023, 289: 116267.
[26] Zhang Z, Feng L, Wang J, et al. Effect of microalloying on wettability and interface characteristics of Zr-based bulk metallic glasses with W substrate. China Foundry, 2024, 21(4): 352–359.
[27] Cheng X, Li F, Yan Z, et al. Effect of Mo addition on the properties of Fe-Co-Zr-W-B bulk metallic glasses. Journal of Non-Crystalline Solids, 2022, 587: 121587.
[28] Guo M, Xue J, Li Y, et al. Effects of Cr addition on structure, magnetic properties and corrosion resistance of a $Fe_{85.5}B_{13}Cu_{1.5}$ nanocrystalline alloy. Journal of Materials Research and Technology, 2024, 30: 2902–2910.
[29] Shen B, Akiba M, Inoue A. Effect of Cr addition on the glass-forming ability, magnetic properties, and corrosion resistance in FeMoGaPCBSi bulk glassy alloys. Journal of Applied Physics, 2006, 100: 043523.
[30] Xu D, Zhou B, Wang Q, et al. Effects of Cr addition on thermal stability, soft magnetic properties and corrosion resistance of FeSiB amorphous alloys. Corrosion Science, 2018, 138: 20–27.
[31] Sun M, Yang Z, Song S, et al. Effect of Cr content on microstructure, mechanical, and corrosion properties of $CoCr_xFeMnNi$ high-entropy alloys fabricated by selective laser melting. Materials Characterization, 2024, 212: 113949.
[32] Heidari E, Atapour M, Obeydavi A. The effect of Cr-content on the corrosion behavior of $Ti_{0.5}Mo_{0.5}CoNiMnCr_x$ high-entropy alloy thin films deposited by direct current magnetron sputtering. Journal of Alloys and Compounds, 2024, 976: 173265.
[33] Zhang S, Shi M, Zhang Z, et al. Influence of metalloid element B on the microstructure and performances of novel FeCoNiVB high-entropy amorphous alloys. Materials Letters, 2024, 362: 136216.
[34] Zeng W, Chen Y, Ye J. Effect of partial substitution of Cr with Co on the properties of $Fe_{35}Ni_{20}Cr_{20-x}Co_xMo_5P_{12}C_4B_4$ high-entropy bulk metallic glasses. Journal of Non-Crystalline Solids, 2024, 625: 122757.
[35] Wu Y, Dai Z, Liu R, et al. Effects of heat treatment on the microstructures and magnetic properties of $Co_{28}Fe_{28}Ni_{19}Si_{13}B_{12}$ high-entropy amorphous toroidal core. Journal of Alloys and Compounds, 2024, 981: 173713.
[36] Du Y, Zhou Q, Pei X, et al. Enhancing the tribological performance of the TiZrHfCuBe high entropy bulk metallic glass by Sn addition. Tribology International, 2022, 171: 107529.
[37] Ding H, Zhang Q, Yao K. Composition design strategy for high entropy amorphous alloys. Materials, 2024, 17: 453.
[38] Guo Q, Xu X, Pei X, et al. Predict the phase formation of high-entropy alloys by compositions. Journal of Materials Research and Technology, 2023, 22: 3331–3339.
[39] Li R, Zhang Y. Entropy and glass formation. Acta Physica Sinica, 2017, 66: 177101.
[40] Narges A, Safdar H, Mohammadiparsa N. Effects of different quenching rate on the various properties of Fe-Si-B amorphous alloy prepared by melt spinning method. Glass Physics and Chemistry, 2023, 49: 617–624.
[41] Zhang S, Zhang Z, Chen C, et al. Experimental investigation of minor Si addition on AlNiYCo multi-principal element alloy: Microstructural characterization, thermal stability and corrosion resistance. Intermetallics, 2022, 151: 107711.
[42] Egbu J, Ohodnicki J, Baltrus J, et al. Analysis of surface roughness and oxidation of FeNi-based metal amorphous nanocomposite alloys. Journal of Alloys and Compounds, 2022, 912: 165155.
[43] Wang R, Shi L, Wu Y, et al. Effects of Mo on the glass forming ability and properties of Fe-B-C-P-Si-Mo bulk metallic glasses. Journal of Non-Crystalline Solids, 2024, 629: 122868.
[44] Zhong X, Zhang Q, Ma M, et al. Mechanical properties and non-isothermal crystallization kinetics of novel Ti-based high-entropy bulk metallic glasses. Journal of Materials Research and Technology, 2023, 23: 5939–5952.
[45] Zhang S, Wei C, Lv J, et al. Non-isothermal crystallization kinetics of the $Zr_{50}Cu_{34}Al_8Ag_8$ amorphous alloy. Materials Letters, 2022, 307: 130996.
[46] Liu Z, Dong X, Li Y, et al. Insights into the structure sustainable evolution and crystallization kinetics of amorphous $Mg_{60}Ni_{30}La_{10}$ alloy. Materials Today Sustainability, 2024, 26: 100718.
[47] Yi X, Feng X, Huang B, et al. The effect of annealing temperatures on the phase constitutes, thermal properties and corrosion behaviors of Ti-Ni-Zr-Cu high entropy alloy thin ribbons. Journal of Alloys and Compounds, 2022, 896: 162947.
[48] Wang L, Zheng Z, Chen Y, et al. The influence of Co on the magnetic properties of Fe-Si-B-Nb-Cu system. Physica B: Condensed Matter, 2023, 660: 414906.
[49] Luo Y, Ke H, Zeng R, et al. Crystallization behavior of $Zr_{60}Cu_{20}Fe_{10}Al_{10}$ amorphous alloy. Journal of Non-Crystalline Solids, 2020, 528: 119728.
[50] Rashidi R, Malekan M, Gholamipour R. Crystallization kinetics of $Cu_{47}Zr_{47}Al_6$ and $(Cu_{47}Zr_{47}Al_6)_{99}Sn_1$ bulk metallic glasses. Journal of Non-Crystalline Solids, 2018, 498: 272–280.
[51] Itoi T, Inoue A. Thermal stability and soft magnetic properties of Co-Fe-M-B (M=Nb, Zr) amorphous alloys with large supercooled liquid region. Materials Transactions, 2000, 41: 1256–1262.
[52] Dong Y, Man Q, Chang C, et al. Preparation and magnetic properties of $(Co_{0.6}Fe_{0.3}Ni_{0.1})_{70-x}(B_{0.811}Si_{0.189})_{25+x}Nb_5$ bulk glassy alloys. Journal of Materials Science: Materials in Electronics, 2015, 26: 7006–7012.
[53] Zhang J, Ma S, Wang H, et al. Effects and mechanisms of Nb and Fe additions on glass-forming ability and magnetic properties of a $Co_{71.5}Gd_{3.5}B_{25}$ metallic glass. Journal of Alloys and Compounds, 2023, 968: 171875.
[54] Li Y, Zhang W, Qi T. New soft magnetic $Fe_{25}Co_{25}Ni_{25}(P, C, B)_{25}$ high entropy bulk metallic glasses with large supercooled liquid region. Journal of Alloys and Compounds, 2017, 693: 25–31.
[55] Li X, Shan G, Pang S, et al. Efficient property-oriented optimization of magnetic high-entropy metallic glasses via a multi-stage design strategy. Applied Materials Today, 2023, 35: 101977.
[56] Zhang Y, Zuo T, Cheng Y, et al. High-entropy alloys with high saturation magnetization, electrical resistivity, and malleability. Scientific Reports, 2013, 3: 1455.
[57] Taghvaei A, Farajollahi R, Bednarčík J, et al. Atomic structure, thermal stability and isothermal crystallization kinetics of novel Co-based metallic glasses with excellent soft magnetic properties. Journal of Alloys and Compounds, 2023, 963: 171271.

[58] Xu S, Wang J, Wang N, et al. Soft magnetic properties and corrosion resistance of the annealed $(Fe_{0.7}Co_{0.15}Ni_{0.15})_{75}B_{21}Nb_4$ metallic glasses. Materials Today Communications, 2021, 26: 101906.
[59] Karaköse E, Keskin M. Microstructures and microhardness evolutions of melt-spun Al-8Ni-5Nd-4Si alloy. Materials Characterization, 2012, 65: 37–47.
[60] Liu C, Zhang Y, Yuan G, et al. Microstructure and properties of ultra-thick Fe-based metallic glass by twin-roll strip casting versus a traditional process. Materials Research Bulletin, 2022, 153: 111878.
[61] Sahoo T, Majumdar B, Srinivas V, et al. Improved magnetoimpedance and mechanical properties on nanocrystallization of amorphous $Fe_{68.5}Si_{18.5}Cu_1Nb_3B_9$ ribbons. Journal of Magnetism and Magnetic Materials, 2013, 343: 13–20.
[62] Shu C, Yao Z, Li X, et al. Microstructure and wear mechanism of $CoCrCuFeNiV_x$ high entropy alloy by sintering and electron beam remelting. Physica B: Condensed Matter, 2022, 638: 413834.
[63] Kumar D. Recent advances in tribology of high entropy alloys: A critical review. Progress in Materials Science, 2023, 136: 101106.
[64] Li W, Xie D, Li D, et al. Mechanical behavior of high-entropy alloys. Progress in Materials Science, 2021, 118: 100777.
[65] Sun J, Shen P, Shang Q, et al. Effects of adding B element on amorphous forming ability, magnetic properties, and mechanical properties of FePBCCu alloy. Acta Physica Sinica, 2023, 72: 206–214.
[66] Shi M, Liu Z, Zhang T. Effects of metalloid B addition on the glass formation, magnetic and mechanical properties of FePCB bulk metallic glasses. Journal of Materials Science & Technology, 2015, 31: 493–497.
[67] Zhang D, Li Q, Sun R, et al. Effect of Mn addition on microstructure and corrosion behavior of AlCoCrFeNi high-entropy alloy. Intermetallics, 2024, 167: 108236.
[68] Zhou J, Kong D. Effects of Ni addition on corrosion behaviors of laser cladded FeSiBNi coating in 3.5% NaCl solution. Journal of Alloys and Compounds, 2019, 795: 416–425.
[69] Ge Y, Cheng J, Mo J, et al. Experimental and DFT studies on corrosion behaviors of laser-cladded $(FeCoNi)_{75-x}Cr_xB_{15}Si_{10}$ high-entropy alloy coatings. Journal of Alloys and Compounds, 2024, 976: 173173.
[70] Xu Z, Zhang H, Du X, et al. Corrosion resistance enhancement of CoCrFeMnNi high-entropy alloy fabricated by additive manufacturing. Corrosion Science, 2020, 177: 108954.
[71] Cai A, Zhou G, Li P, et al. Mechanical, wetting and corrosion properties of a Zr-based amorphous alloy composite consolidated by spark plasma sintering. Journal of Non-Crystalline Solids, 2023, 621: 122648.
[72] Chang W, Wang X, Qian H, et al. Effect of Sn addition on microstructure, hardness and corrosion behavior of $CoCrFeNiSn_x$ high entropy alloys in chloride environment. Corrosion Science, 2024, 227: 111808.
[73] Wang Y, Li G, Qi H, et al. Effect of non-metallic carbon content on the microstructure and corrosion behavior of AlCoCrFeNi high-entropy alloys. Intermetallics, 2024, 166: 108181.
[74] Wu H, Wang L, Zhang S, et al. Corrosion and cavitation erosion behaviors of laser clad FeNiCoCr high-entropy alloy coatings with different types of TiC reinforcement. Surface and Coatings Technology, 2023, 471: 129910.
[75] Wu Z, Li B, Chen M, et al. Tailoring magnetic property and corrosion resistance of FeCoNiCuAl high-entropy alloy with Ce additive. Journal of Alloys and Compounds, 2022, 901: 163665.
[76] Han Y, Chang C, Zhu S, et al. Fe-based soft magnetic amorphous alloys with high saturation magnetization above 1.5 T and high corrosion resistance. Intermetallics, 2014, 54: 169–175.
[77] Liu C, Gao Y, Chong K, et al. Effect of Nb content on the microstructure and corrosion resistance of $FeCoCrNiNb_x$ high-entropy alloys in chloride ion environment. Journal of Alloys and Compounds, 2023, 935: 168013.
[78] Zhang S, Gao Y, Zhang Z, et al. Research progress in corrosion resistance of high-entropy metallic glasses. Journal of Materials Engineering, 2021, 49: 44–54.
[79] Feng K, Zhang Y, Li Z, et al. Corrosion properties of laser cladded CrCoNi medium entropy alloy coating. Surface and Coatings Technology, 2020, 397: 126004.
[80] Luo H, Zou S, Chen Y, et al. Influence of carbon on the corrosion behaviour of interstitial equiatomic CoCrFeMnNi high-entropy alloys in a chlorinated concrete solution. Corrosion Science, 2020, 163: 108287.
[81] Zhang C, Li Q, Xie L, et al. Development of novel Fe-based bulk metallic glasses with excellent wear and corrosion resistance by adjusting the Cr and Mo contents. Intermetallics, 2023, 153: 107801.